I&EC research
Industrial & Engineering Chemistry Research

Article

Cite This: Ind. Eng. Chem. Res. 2017, 56, 12184-12191

pubs.acs.org/IECR

Characterization and Modeling of the Operating Curves of Membrane Microseparators

Lu Yang,[†] Nopphon Weeranoppanant,[†,‡] and Klavs F. Jensen*[,†]

[†]Department of Chemical Engineering, Massachusetts Institute of Technology, Cambridge, Massachusetts 02139, United States
[‡]Department of Chemical Engineering, Faculty of Engineering, Burapha University, Chonburi 20131, Thailand

Supporting Information

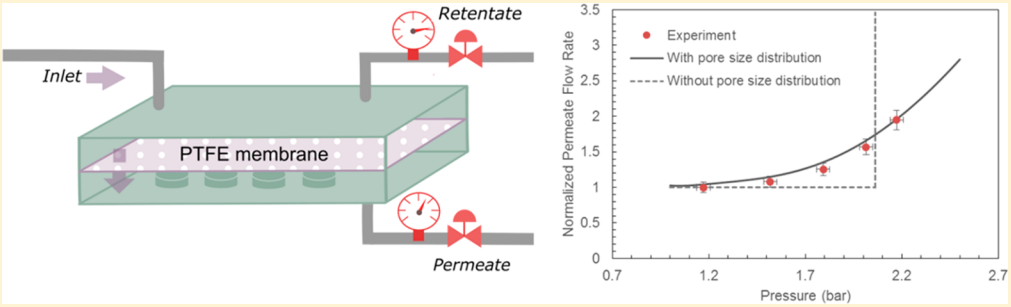

ABSTRACT: The membrane microseparator is a milliliter-scale flow chemistry module that continuously separates a biphasic flow through a PTFE microporous membrane. It has found a wide range of applications in the continuous manufacturing of active pharmaceutical ingredients and fine chemicals, especially those involving multiple synthetic steps. Yet, the accurate prediction and control of the pressure balance needed for successful phase separations is technically challenging. In this article, we present systematic modeling of the operating ranges of the membrane microseparator. We characterize the retention and breakthrough phenomena of the device and develop two new analytic models for retention and breakthrough by taking into consideration the tortuosity factor and pore size distribution. The new models are shown to be better predictors of the experimental results than the original theoretical models based on the simple Young−Laplace equation and the straight-channel Hagen−Poiseuille equation.

1. INTRODUCTION

With the rapid development of flow chemistry technology in the past two decades, a wide variety of microfluidic modules have been developed that facilitate the execution of chemical synthesis and workup on the microscale.[1] As a ubiquitous unit operation, continuous multiphase separation has become an indispensable component downstream of multiphase reactors in microscale flow chemistry applications. Because of the decrease in length scale, phase separation by gravity is no longer feasible on the microscale. Instead, researchers have exploited the dominant capillary force to achieve successful continuous separations driven by differences in the wetting characteristics of the two fluids. Specifically, Gunther et al. fabricated a capillary microseparator that included an array of micrometer-scale capillaries as side channels that were able to absorb the wetting phase while leaving the nonwetting phase in the main channel.[2] Similar designs have since been developed by researchers to perform a wide array of tasks, including reaction workup, extraction, and demulsification.[3−7]

Although the capillary microseparator enjoys many benefits, including well-defined straight pores that prevent clogging and facilitate computational fluid dynamics (CFD) modeling, the device is rather difficult to scale up to accommodate higher throughput. The maximum permeate removal flow rate through the capillary microseparator is equal to the flow rate of the wetting fluid through each capillary, Q_{cap}, multiplied by the total number of capillaries, n. Q_{cap} is directly proportional to the pressure drop across the capillary, which is limited by the breakthrough pressure threshold.[8] Therefore, without much flexibility around Q_{cap}, the permeate removal flow rate scales linearly with the total number of capillaries, n. For higher flow rates, it becomes uneconomical or even impractical to fabricate microseparator devices with hundreds or thousands of capillaries in parallel.

Separators employing microporous membranes offer alternatives to microcapillary arrays for achieving separations on a larger scale. The application of microporous membranes as phase separators and contactors originated decades ago in the field of analytical chemistry. Nord spearheaded the use of the microporous membrane as a sample preparation method for an extraction manifold in flow injection analysis (FIA).[9] He also tested a wide array of membrane materials and recommended the use of a polytetrafluoroethylene (PTFE) membrane with a

Received: August 2, 2017
Revised: October 2, 2017
Accepted: October 3, 2017
Published: October 3, 2017

DOI: 10.1021/acs.iecr.7b03207
Ind. Eng. Chem. Res. 2017, 56, 12184−12191

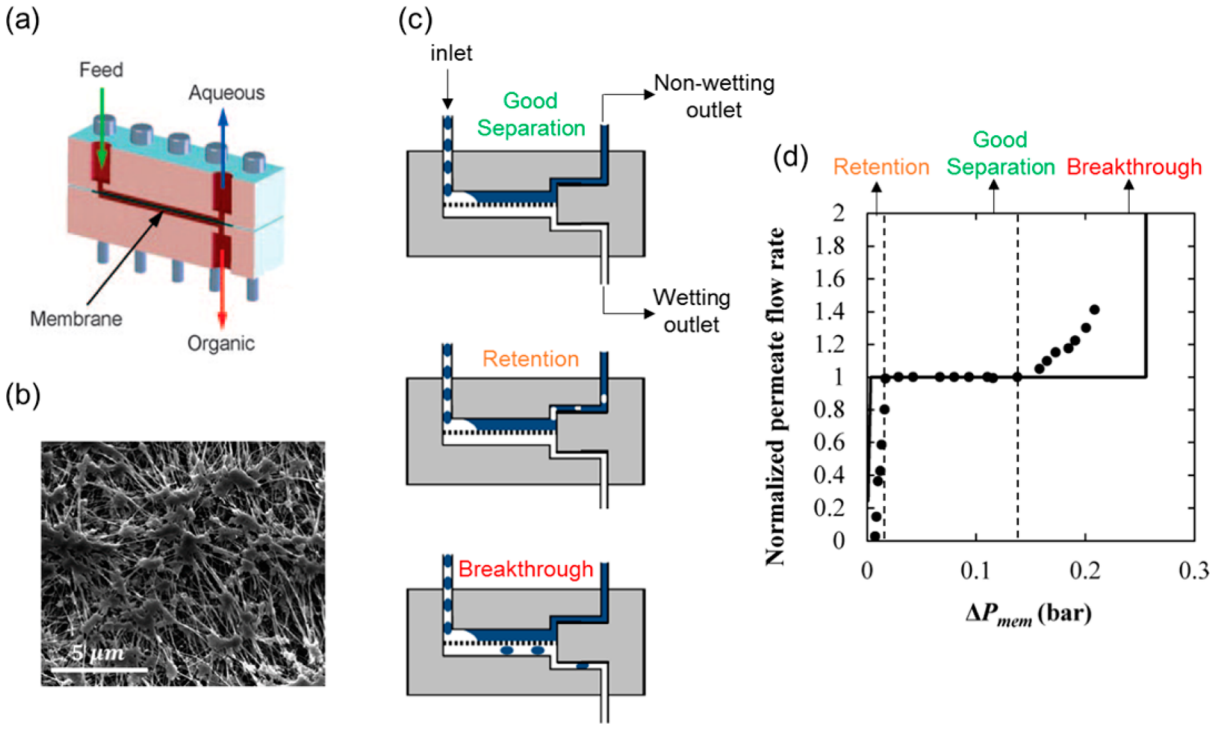

Figure 1. (a) Scheme showing the composition of a membrane separator, where there is one biphasic feed inlet and two outlets, one for the aqueous stream and one for the organic stream.[13] (b) SEM image of the active surface of the PTFE membrane.[15] (c) Schemes demonstrating the three operating modes of the membrane separator.[14] (d) Comparison of the theoretical limit (solid line) and experimental measurements (circles). The retention, complete separation, and breakthrough regimes are indicated by yellow, green, and red text, respectively. In the retention and complete separation regimes, the permeate phase consists solely of the organic phase, whereas in the breakthrough regime, the permeate is a mixture of organic and aqueous phases. The normalized permeate flow rate is the ratio of the permeate flow rate to the incoming organic-phase flow rate, and its value should be equal to 1 when complete separation occurs.[14]

polyethylene support for future studies, because of its high durability and solvent compatibility. Valcarcel and Luque de Castro reviewed the application of microporous membranes as a tool for continuous separation for FIA,[10] and Jonsson and Mathiasson summarized the use of membrane technology in sample enrichment as applied to analytical methods, including FIA, gas chromatography (GC), and high-performance liquid chromatography (HPLC).[11] Following this line of work, Cai et al. fabricated a membrane-based contactor in a microfluidic chip, in which the aqueous and organic phases each flow on one side of the microporous membrane, so that the analyte in the aqueous phase can be extracted into the organic phase without the need for further separation.[12]

Kralj et al. employed microporous PTFE membranes to replace microcapillary arrays in achieving phase separations in flow chemistry applications (Figure 1a).[13] Compared to microcapillary separators, the membrane separator enjoys several distinct advantages: (1) The membrane can be easily scaled up using similar configurations and can accommodate a much wider range of flow rates. Although microseparators are mostly designed for lab-on-a-chip demonstrations and microchemical assays, the membrane separator is compatible with larger-scale flow chemistry applications and has promising applications in small-scale production. (2) The membrane-based separator is easier to assemble because it eliminates the need for the microfabrication of each capillary. (3) The membrane-based separator also provides better reusability, as a membrane can easily be substituted if it becomes clogged, fouled, or otherwise dysfunctional, whereas the entire capillary microseparator chip would have to be replaced under the same circumstances. (4) The membrane separator has much smaller pores (0.1−10 μm) than the capillary separator (20 μm), which is essential for the separation of systems with low interfacial tensions.

There are also three distinct operating regimes in which the membrane separator (Figure 1c) operates, the retention regime, the complete separation regime, and the breakthrough regime.[14] The three regimes are controlled by one variable, the pressure drop across the membrane, ΔP_{mem}. If ΔP_{mem} is too low, the pressure gradient is not sufficient to push all of the organic phase through the PTFE membrane, thus resulting in the retention of the organic phase in the aqueous stream. This pressure threshold is called the retention pressure threshold, $\Delta P_{retention}$. On the other hand, if ΔP_{mem} is too high, both the organic phase and the aqueous phase permeate through the membrane, resulting in the contamination of the organic stream by the aqueous phase. This pressure limit is called the breakthrough pressure threshold, $\Delta P_{breakthrough}$. When ΔP_{mem} is in the range $\Delta P_{retention} < \Delta P_{mem} < \Delta P_{breakthrough}$, complete separation takes place, where the biphasic flow from the inlet is continuously separated into an organic phase and an aqueous phase.

Kralj et al. first designed a polycarbonate module containing a PTFE membrane to demonstrate the separation concept and then fabricated a silicon device that integrated a multiphase mixer, a contactor, and a separator into a single chip.[13] Since then, the membrane microseparator has been applied by many researchers as an indispensable workup tool for achieving multistep continuous syntheses.[16−26] For instance, the membrane separator was used by Sahoo et al. to integrate

DOI: 10.1021/acs.iecr.7b03207
Ind. Eng. Chem. Res. 2017, 56, 12184−12191

three chemical reactions continuously with separation steps between the reactions.[27] Alimuddin et al. employed a membrane separator to design an automated, high-throughput method for measuring the oil/water distribution coefficients of molecules to replace the traditional shake-flask method.[28] Hartman and co-workers expanded the application of membrane separators to the field of microscale distillation, adding yet another useful module to the toolbox of continuous flow chemistry synthesis.[29,30] Heider et al. further demonstrated the scalability and practicality of the membrane separator by using scaled-up membrane separators in the continuous synthesis of a pharmaceutical product, where each separator unit was equipped to handle flow rates between 10 and 1000 mL/h and the membrane ran successfully for 100 h before fouling occurred.[31] Based on the multitude of applications, Cervera-Padrell et al. evaluated different liquid−liquid separation technologies in the context of large-scale industrial applications for continuous pharmaceutical production and concluded that the microporous membrane separator is one of the most suitable, flexible, and robust devices for this purpose.[32]

Despite its versatility and adaptability, an inevitable difficulty with the inline application of membrane separators is the stringent requirement for pressure control. For the device to function properly, the pressures at both the wetting and nonwetting outlets must be maintained meticulously, as deviations in each value would result in errors in ΔP_{mem}, thus hindering the smooth operation of the device. This is especially difficult given that the separator, when used in the middle of a sequence of flow chemistry modules, is frequently subject to pressure fluctuations from upstream and downstream. In addition, two sets of pressure control valves take up extra space and make the system cumbersome, especially when multiple separation steps are involved. To address this problem, Adamo et al. designed a membrane separator device coupled with a deformed diaphragm that provided a constant pressure difference across the membrane, regardless of the outlet conditions.[14] Through the fine-tuning of the configuration of the diaphragm, consistent and complete separation performance could be guaranteed. The same module has been employed as an integral part of a refrigerator-sized "flow chemistry factory" to synthesize and formulate pharmaceuticals on demand[33] and has also been used as the separator in the continuous solvent-free oxidation of alcohols.[34] Moreover, the independent nature of the units enabled their integration into countercurrent extraction.[35]

Regardless of the pressure control mechanism, the key issue in operating a membrane separator is to understand the pressure ranges over which complete separation occurs. Although theoretical expressions exist for the breakthrough and retention thresholds, based on the capillary flow model, they largely fail to predict the operating ranges of the membrane separator (Figure 1d).[14] This behavior results from the polydispersity and tortuosity of the fluid path in the membrane (Figure 1b), as compared to the well-defined micromachined straight channels in the capillary separator. The polydispersity of the membrane pore sizes reduces the breakthrough pressure threshold, as breakthrough occurs through the largest pores, and consequently narrows the operating window. In addition, the tortuous fluid path in the membrane increases the flow resistance and raises the retention pressure limits compared to those of the straight and uniform channels in microfabricated capillary separators. This discrepancy between the theoretical framework and experimental measurements was observed by Adamo et al. (Figure 1d).[14] Specifically, whereas the theoretical model is able to qualitatively capture the three operating regimes of the device, it tends to underpredict the onset of retention and to overpredict the start of breakthrough, thus overestimating the pressure range for complete separation.

Recognizing the strong need for an increased understanding of the operation this device, we sought to establish an analytic model for understanding and predicting the operating ranges of the membrane microseparator based on systematic experimental characterization. In this article, we present the derivation of a new set of analytic models, compare the results of the new model with those of the original ones, and demonstrate the use of the new model in predicting the performance of the membrane separator.

2. METHODS

2.1. Experimental Measurements. The membrane testing unit (Figure 2) was machined in perfluorinated polymers

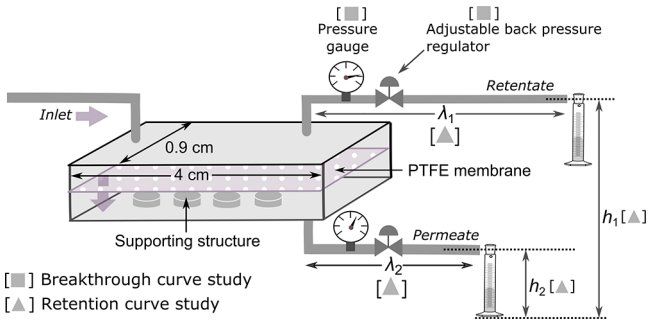

Figure 2. Membrane testing unit used to study breakthrough and retention phenomena.

[high-density polyethylene (HDPE)] and was embedded in a metal shell for higher pressure rating. The membrane used was made of PTFE with a nominal pore diameter of 1.0 μm (Pall Corporation, New York). It had a supporting layer of PTFE. O-rings coated with fluorinated ethylene−propylene (FEP) were used to provide a leak proof seal. The membrane area was 4.0 × 0.8 cm^2. Subtraction of the areas occupied by the supporting islands through which no permeation occurred from this overall area gave the active membrane area as 157 mm^2. This unit was used for both breakthrough and retention studies. To generate a breakthrough curve, the unit was installed with pressure gauges and back-pressure regulators (BPRs) on the two outlets (Figure 2, highlighted in red). Two liquid−liquid (immiscible) combinations were tested: (a) water/toluene, (b) water/hexane. The two BPRs were connected to adjustable compressed gas tanks so that the BPR set points could be changed dynamically during the experiments. The two immiscible phases, delivered into the system by peristaltic pumps, were mixed in a T-junction and then introduced into the membrane testing unit. Because of high hydrophobicity of the membrane, the organic phase tended to wet and permeate through the membrane, whereas the aqueous phase would be retained. However, provided a sufficiently high pressure difference across the membrane, the aqueous phase could partially, or even fully, permeate through the membrane too. By adjusting the regulators of the compressed gas tanks, we could set the pressures on the BPRs. At each adjustment, the setup was allowed to equilibrate as the reading on the gauges stopped

DOI: 10.1021/acs.iecr.7b03207
Ind. Eng. Chem. Res. 2017, 56, 12184−12191

changing. We then recorded the actual pressures of the two gauges and used these values to calculate the pressure difference between the two sides of the membrane (ΔP_{mem}). The flow rates of both the aqueous and organic phases in the two outlets were measured simultaneously using graduated cylinders and timers. Based on repeated runs under the same experimental conditions, we were able to quantify the random errors in this experimental setup. For the breakthrough curve measurements, the relative standard error of ΔP_{mem} was 2.5%, and that of the normalized permeate flow rate was 7.1%, which was likely due to the pulsatile nature of the pump.

In this testing unit, the retention occurred at very low pressure differences (<0.1 psi), which was beyond the resolution of the pressure gauges and the BPRs available. Because the essence of the retention phenomenon is the flow of wetting fluid through the membrane under low pressures, we instead employed a single-phase flow (hexane or toluene) and measured its flow rate as a function of pressure. The pressure was controlled by manipulating the hydrostatic pressures of the two outlets (Figure 2, highlighted in blue). We varied the heights of the two outlets and measured the actual flow rates of the two outlets using graduated cylinders and timers. The pressure difference between the two sides of the membrane was then determined as

$$\Delta P_{mem} = P_1 - P_2 = \rho_{org} g(h_1 - h_2) + \frac{8\mu_{org}}{\pi r_{tube}^4}(\lambda_1 Q_1 - \lambda_2 Q_2) \quad (1)$$

where ρ_{org} and μ_{org} are density and viscosity of the solvent, r_{tube} is the radius of the outlet tubing, h_1 and h_2 are the height of the outlets from a reference point, λ_1 and λ_2 are the corresponding lengths of the tubing from the testing unit to the outlets, and Q_1 and Q_2 are the corresponding volumetric flow rates of retentate and permeate through the outlets. Subscripts 1 and 2 indicate the retentate and permeate outlets, respectively. For the retention measurements, the relative standard error of ΔP_{mem} was 5%, and that of the normalized permeate flow rate was 7.1%.

2.2. Mathematical Model. *2.2.1. Single-Phase Flow through the Membrane under the Retention Limit.* The retention limit occurs when there is just enough pressure to propel the organic phase through the membrane, and if the pores were straight and uniform in size and did not intersect, this limit could be described by the Hagen–Poiseuille equation

$$\Delta P_{retention,theoretical} = \Delta P_{H-P} = \frac{8\mu_{org} L Q_{org}}{n\bar{R}^4} \quad (2)$$

Here, L is the thickness of the membrane, Q_{org} is the flow rate of the organic phase through the membrane, n is the total number of capillaries, and $\bar{R}$ is the average radius of the membrane pores.

In the ideal case, this correlation could be applied to the single-phase retention-like measurements described in the Experimental Measurement section. However, eq 2 alone is insufficient to reflect the relationship between the wetting-phase flow rate and the pressure drop below the retention limit, as shown in Figure 1d. In Figure 1d, the measured ΔP_{mem} values are much higher than the predictions. Therefore, as pointed out previously, an additional tortuosity factor, C_{tor}, needs to be added to account for the complex geometry in the membrane structure. The tortuosity factor C_{tor} is defined as the average ratio between the length over which the fluid travels through the membrane and the membrane thickness,[36,37] which also becomes an important input parameter for the breakthrough curve model as well

$$\Delta P_{retention,theoretical} = \frac{8C_{tor}\mu_{org} L Q_{org}}{n\bar{R}^4} \quad (3)$$

2.2.2. Breakthrough Curve. In a capillary microseparator, the breakthrough point is simply dictated by the Young–Laplace equation

$$\Delta P_{breakthrough} = \Delta P_{Y-P} = \frac{2\sigma \cos\theta}{\bar{R}} \quad (4)$$

where σ is the interfacial tension between the two immiscible fluids and θ is the contact angle.

However, as shown in the breakthrough regime in Figure 1d, actual breakthrough in the membrane separator occurred much earlier and at a much more gradual rate because of the wide distribution of pore sizes in the PTFE membrane. We therefore define a pore size distribution function, $n(R)$, such that $\int_{R_1}^{R_2} n(R)\,dR$ represents the number of pores between radii of R_1 and R_2

$$N \text{ (from } R_1 \text{ to } R_2) = \int_{R_1}^{R_2} n(R)\,dR \quad (5)$$

During breakthrough, each ΔP_{mem} value corresponds to a threshold membrane pore radius, $R_{\Delta P_{mem}}$, meaning that, under this specific pressure difference, breakthrough occurs through pores with radii that are equal to or larger than $R_{\Delta P_{mem}}$

$$\Delta P_{mem} = \frac{2\sigma}{R_{\Delta P_{mem}}} \quad (6)$$

Because of the high hydrophobicity of the PTFE membrane, we assumed the contact angle of the organic phase to be zero. Ładosz and von Rohr provide a detailed discussion on the impact of contact angle for capillary separators.[8]

Therefore, the total aqueous flow rate that passes through the membrane under ΔP_{mem} is the sum of thhe flow rates through all of these pores. The differential aqueous flow rate, $dQ_{aq,perm}$, through pores with radii between R_i and $R_i + dR$ ($R_i > R_{\Delta P_{mem}}$) can be expressed using the Hagen–Poiseuille equation modified with the tortuosity factor

$$dQ_{aq,perm} = \frac{\pi}{8C_{tor}\mu_{aq} L}\Delta P_{mem} n(R_i) R_i^4\,dR \quad (7)$$

Note here that the C_{tor} value obtained from the retention model also applies to the breakthrough model.

Integrating from the smallest available pore, $R_{\Delta P_{mem}}$, to infinity, we obtain

$$Q_{aq,perm} = \frac{\pi}{8C_{tor}\mu_{aq} L}\Delta P_{mem}\int_{R_{\Delta P_{mem}}}^{\infty} n(R)R^4\,dR \quad (8)$$

Also note that

$$Q_{aq,perm} = Q_{total,perm} - Q_{org} \quad (9)$$

where $Q_{aq,perm}$ is the aqueous flow rate through the membrane, $Q_{total,perm}$ is the total permeate flow rate, and Q_{org} is the flow rate of the organic phase.

Substitution of eq 6 into eq 8 gives

DOI: 10.1021/acs.iecr.7b03207
Ind. Eng. Chem. Res. 2017, 56, 12184–12191

Table 1. Comparison of the Original Model and the New Model for Characterizing Retention and Breakthrough Phenomena in Membrane Separators

model	retention	breakthrough
original	$\Delta P_{\text{retention}} = \frac{8\mu_{\text{org}} L Q_{\text{org}}}{n\bar{R}^4}$	If $\Delta P > \frac{2\sigma\cos\theta}{\bar{R}}$, then both phases flow through the capillaries
new[a]	$\Delta P_{\text{retention}} = \frac{8C_{\text{tor}}\mu_{\text{org}} L Q_{\text{org}}}{n\bar{R}^4}$	$Q_{\text{aq,perm}} = \frac{\pi}{8C_{\text{tor}}\mu_{\text{aq}} L}\Delta P_{\text{mem}} \int_{2\sigma/\Delta P_{\text{mem}}}^{\infty} n(R)R^4\, \text{d}R$

[a]With modifications for tortuosity and pore size distribution.

$$Q_{\text{aq,perm}} = \frac{\pi\sigma}{4C_{\text{tor}}\mu_{\text{aq}} L}\frac{1}{R_{\Delta P_{\text{mem}}}}\int_{R_{\Delta P_{\text{mem}}}}^{\infty} n(R)R^4\, \text{d}R \tag{10}$$

Moving $R_{\Delta P_{\text{mem}}}$ to the left-hand side and differentiating with respect to R, we obtain

$$\frac{\text{d}(Q_{\text{aq,perm}} R_{\Delta P_{\text{mem}}})}{\text{d}R_{\Delta P_{\text{mem}}}} = -\frac{\pi\sigma}{4C_{\text{tor}}\mu_{\text{aq}} L} n(R_{\Delta P_{\text{mem}}}) {R_{\Delta P_{\text{mem}}}}^4 \tag{11}$$

Therefore

$$n(R) = -\frac{4C_{\text{tor}}\mu_{\text{aq}} L}{\pi\sigma R^4}\frac{\text{d}(Q_{\text{aq,perm}} R_{\Delta P_{\text{mem}}})}{\text{d}R_{\Delta P_{\text{mem}}}} \tag{12}$$

From the experiments, we directly obtained $Q_{\text{aq,perm}}$ and ΔP_{mem}. We could then apply eq 6 to transform ΔP_{mem} into the corresponding value of $R_{\Delta P_{\text{mem}}}$, which yielded a series of data points linking $Q_{\text{aq,perm}}$ and $R_{\Delta P_{\text{mem}}}$. Note that, to use eq 12 to obtain $n(R)$, it is necessary to have a continuous and differentiable function for $Q_{\text{aq,perm}} = f(R_{\Delta P_{\text{mem}}})$. Therefore, we applied polynomial fitting to the $Q_{\text{aq,perm}}$–$R_{\Delta P_{\text{mem}}}$ data set to obtain a smooth functional form that could then be used in eq 12.

In addition, whereas the breakthrough curve can be measured under various fluid combinations and flow rates, the calculated pore size distribution function, $n(R)$, should also remain the same as long as the same membrane device was used. This inspired us to reformulate the model to consolidate all of the experimental data points into one calculation, regardless of the fluid choices and operating conditions. This was achieved by rearranging eq 8 so that all of the data points, regardless of interfacial tension and flow rates, could be consolidated into a single chart

$$\frac{Q_{\text{aq,perm}}}{\Delta P_{\text{mem}}} = \frac{\pi}{8C_{\text{tor}}\mu_{\text{aq}} L}\int_{R_{\Delta P_{\text{mem}}}}^{\infty} n(R)R^4\, \text{d}R \tag{13}$$

Because the right-hand side of eq 13 is a function of only R, all of the data points should follow the same trend line on a plot of $\frac{Q_{\text{aq,perm}}}{\Delta P_{\text{mem}}}$ versus R.

Further differentiating and rearranging eq 13, we obtained

$$n(R) = -\frac{8C_{\text{tor}}\mu_{\text{aq}} L}{\pi R^4}\frac{\text{d}\left(\frac{Q_{\text{aq,perm}}}{\Delta P_{\text{mem}}}\right)}{\text{d}R_{\Delta P_{\text{mem}}}} \tag{14}$$

This is the final expression for calculating $n(R)$ based on multiple sets of experimental measurements.

Once $n(R)$ is known, it is then possible to reverse the analysis to predict the shape of the breakthrough curve under any given fluid combination and flow rates using the equation

$$Q_{\text{aq,perm}} = \frac{\pi}{8C_{\text{tor}}\mu_{\text{aq}} L}\Delta P_{\text{mem}}\int_{2\sigma/\Delta P_{\text{mem}}}^{\infty} n(R)R^4\, \text{d}R \tag{15}$$

Note that the only unknown on the right-hand side of eq 15 is ΔP_{mem}. Therefore, given ΔP_{mem}, it is possible to calculate the corresponding $Q_{\text{aq,perm}}$ value directly, which forms the predictive breakthrough curve. The model for predicting the pressure ranges of the membrane microseparator presented above is in many ways analogous to that used for capillary microseparators,[38] as both devices operate based on the capillary pressure. However, there are two major differences:

(1) The pores in the PTFE membrane are not straight channels, but rather a tortuous network of interconnecting void structures, which increases flow resistance through the membrane. Therefore, when the Hagen–Poiseuille equation is employed to calculate pressure drop across the membrane, the additional tortuosity factor must be taken into consideration.

(2) The pores in the PTFE membrane have a wide distribution in diameter, unlike the uniformly sized channels in the capillary separator, which changes the onset of the breakthrough phenomenon and the shape of the breakthrough curve.

Table 1 summarizes and compares the original models with the new models proposed in this work that incorporate the effects of the tortuosity and the pore size distribution.

3. RESULTS AND DISCUSSION

3.1. Retention Phenomenon Modeling. To formulate the new model, we started by performing a series of one-phase retention-like measurements to understand the characteristics of flow through the membrane, recording the flow rate of the permeated organic phase as a function of the cross-membrane pressure difference. The experimental results are shown in Figure 3a. We were then able to analyze those data points within the framework of eq 3. To obtain an accurate estimation of the tortuosity factor, it is necessary to include as many data points as possible. By plotting ΔP_{mem} as the y axis and plotting the product of Q_{org} and μ_{org} as the x axis, we were able to combine all of the data points covering two solvents (toluene and hexane) and three different flow rates into a single line (Figure 3b). As expected, the data points have a high linear correlation ($R^2 = 0.94$). According to eq 3, the slope is $\frac{8C_{\text{tor}}L}{n\bar{R}^4}$, where the only unknown is C_{tor}. By performing linear regression, we calculated that the tortuosity factor of the membrane, C_{tor}, is equal to 3.52 ± 0.14. We also compared this new model with the original Hagen–Poiseuille expression without the tortuosity factor (Figure 3b). It is evident that the tortuosity modification is crucial in accurately capturing the retention behavior of the membrane. The calculated tortuosity

DOI: 10.1021/acs.iecr.7b03207
Ind. Eng. Chem. Res. 2017, 56, 12184–12191

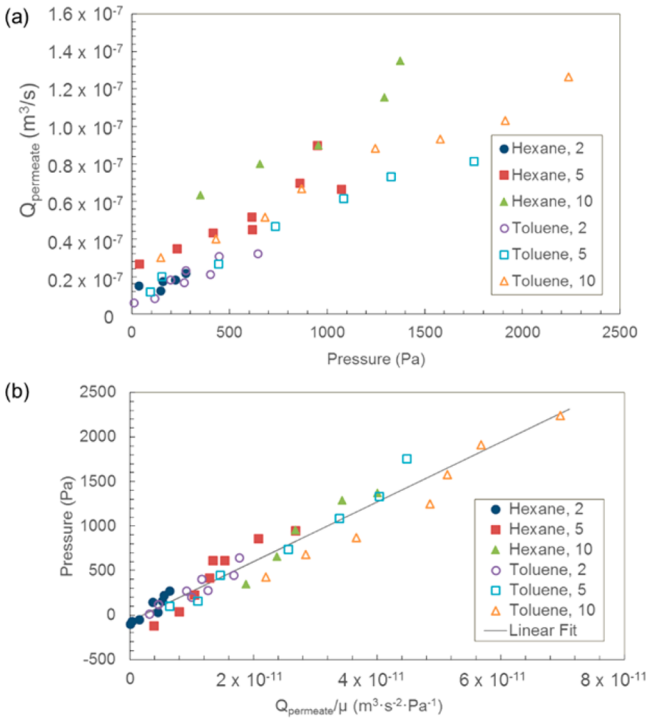

Figure 3. (a) Experimental measurements of retention using the wetting phase (hexane or toluene) at three flow rates: 2, 5, and 10 mL/min. (b) Comparison between the new model and the original Hagen–Poiseuille equation, showing that the new model with the tortuosity modification is able to describe the experimental measurements accurately.

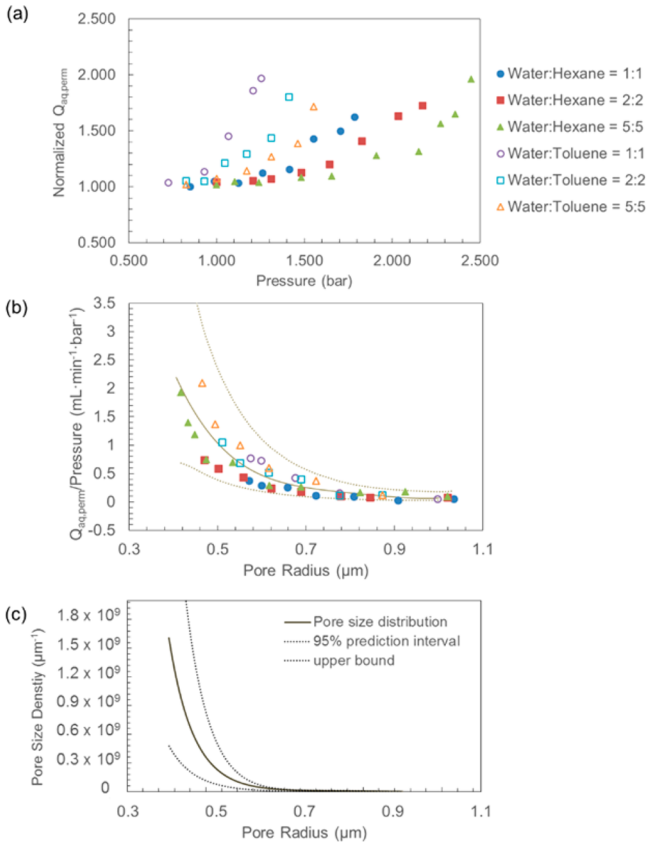

Figure 4. (a) Experimental measurements of the breakthrough curve using both water/hexane and water/toluene at three flow-rate combinations: 1 mL/min/1 mL/min, 2 mL/min/2 mL/min, and 5 mL/min/5 mL/min. (b) Plot of $\frac{Q_{aq,perm}}{\Delta P_{mem}}$ versus R that consolidates all of the experimental measurements into a single trend. (c) Pore size distribution function $n(R)$ calculated from panel b.

factor then becomes an important input that feeds into the breakthrough curve model.

3.2. Breakthrough Curve Modeling. *3.2.1. Calculating Pore Size Distribution.* To understand and model the breakthrough curve, we started by conducting a series of experimental measurements of the breakthrough behavior of the membrane separator using two fluid combinations (water/toluene and water/hexane) at different flow rates (between 1 and 5 mL/min for each phase). The experimental data are presented in Figure 4a, where the y axis is the normalized flow rate of the aqueous phase that permeated through the membrane, namely, $\frac{Q_{aq,perm}}{Q_{org}}$. This value should be equal to zero during complete separation and any positive value indicates the occurrence of breakthrough.

As discussed in section 2.2.2 and shown in eq 13, it is possible to consolidate all of the data points into one single curve by plotting $\frac{Q_{aq,perm}}{\Delta P_{mem}}$ as a function of the corresponding value of $R_{\Delta P_{mem}}$. Indeed, as shown in Figure 4b, all of the data points line up well along the curve, to which we fitted a fifth-order polynomial (R^2 = 0.80). Based on eq 14, the pore size distribution function, $n(R)$, was then calculated as shown in Figure 4c. With $n(R)$ known, we were then enable to make predictions about the shape of the breakthrough curve under other conditions. We also compared the calculated $n(R)$ curve with measurement results obtained using mercury porosimetry and capillary flow porometry. For detailed results and a discussion of this comparison, please refer to the Supporting Information.

3.2.2. Model Predictions. The purpose of extracting the pore size distribution function is to predict the breakthrough curve of the separator under other conditions. With a known $n(R)$ distribution, it is then possible to calculate the predicted permeate flow rate as a function of pressure in the breakthrough regime. For demonstration purposes, we chose to model the water/hexane and water/toluene systems at a flow rate of 3 mL/min for both the aqueous and organic phases in both cases. Following eq 15, we derived their expected breakthrough curves, as shown by the solid lines in Figure 5. The predictions of the old model, that is, the Young–Laplace expression of eq 4, are also plotted in this figure as dashed lines. The predictions of both the new model and the old model are compared with data points collected from experiments under the same conditions. As shown in Figure 5, the new model is more accurate than the old model in predicting the breakthrough behavior of the device. The new model can thus be applied in the same fashion to other fluid combinations, flow rates, and device configurations to predict the operating curves of the device under new conditions.

4. CONCLUSIONS

A systematic study of the three operating regimes of the membrane microseparator was presented by combining experimental measurements and analytical derivations. On the experimental side, the retention and breakthrough phenomena

DOI: 10.1021/acs.iecr.7b03207
Ind. Eng. Chem. Res. 2017, 56, 12184–12191

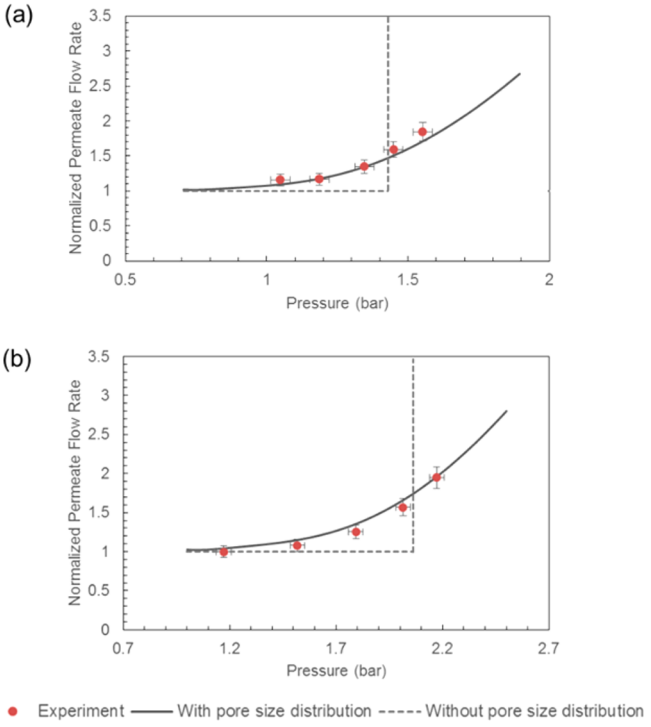

Figure 5. Comparisons between model predictions (solid line) and experimental measurements (red circles, with error bars) for (a) water/hexane and (b) water/toluene biphasic flows with a flow rate of 3 mL/min for each phase.

of a membrane separator were measured at multiple flow rates. Based on the experimentally measured operating curves, a new theoretical framework was developed that included a tortuosity factor and a pore size distribution function to account for the complex inner microstructure of the membrane. The calculated tortuosity factor and pore size distribution were applied to make predictions about the breakthrough curves of the membrane under new conditions, and the model results were shown to be accurate predictions of the experimental measurements. In the future, the models presented in this work could be used to increase the efficiency of process development involving membrane separators by making accurate predictions about the operating behaviors of such devices.

■ ASSOCIATED CONTENT

Supporting Information

The Supporting Information is available free of charge on the ACS Publications website at DOI: 10.1021/acs.iecr.7b03207.

Comparison with other pore size distribution measurements and experimental methods (PDF)

■ AUTHOR INFORMATION

Corresponding Author

*E-mail: kfjensen@mit.edu.

ORCID

Klavs F. Jensen: 0000-0001-7192-580X

Notes

The authors declare no competing financial interest.

■ ACKNOWLEDGMENTS

We thank Novartis-MIT Center for Continuous Manufacturing for financial support.

■ ABBREVIATIONS

C_{tor} = tortuosity factor
h = height of an outlet from a reference point, m
L = thickness of the PTFE membrane, m
$\Delta P_{breakthrough}$ = pressure difference that caused the onset of the breakthrough phenomenon, Pa
ΔP_{H-P} = pressure drop calculated from the Hagen−Poiseuille equation, Pa
ΔP_{mem} = pressure drop across the membrane, Pa
$\Delta P_{retention}$ = pressure difference that caused the onset of the retention phenomenon, Pa
ΔP_{Y-P} = pressure difference calculated from the Young−Laplace equation, Pa
Q = volumetric flow rate, m^3/s
R = pore radius, m
r_{tube} = radius of the outlet tubing radius of the outlet tubing, m

Greek Letters

λ = length of the tubing from the testing unit to an outlet in Figure 2, m
μ = viscosity, Pa·s
ρ = density, kg/m3
σ = interfacial tension between two immiscible fluids, N/m
θ = contact angle of the wetting phase

Subscripts and Superscripts

1 = outlet 1 in Figure 2
2 = outlet 2 in Figure 2
aq = aqueous phase
org = organic phase
perm = permeate phase
total = total flow rate

■ REFERENCES

(1) Jensen, K. F. Flow chemistry—Microreaction technology comes of age. *AIChE J.* **2017**, *63*, 858−869.
(2) Gunther, A.; Jhunjhunwala, M.; Thalmann, M.; Schmidt, M. A.; Jensen, K. F. Micromixing of Miscible Liquids in Segmented Gas-Liquid Flow. *Langmuir* **2005**, *21*, 1547−1555.
(3) Angelescu, D. E.; Mercier, B.; Siess, D.; Schroeder, R. Microfluidic Capillary Separation and Real-Time Spectroscopic Analysis of Specific Components from Multiphase Mixtures. *Anal. Chem.* **2010**, *82*, 2412−2420.
(4) Assmann, N.; Kaiser, S.; von Rohr, P. R. Supercritical extraction of vanillin in a microfluidic device. *J. Supercrit. Fluids* **2012**, *67*, 149−154.
(5) Assmann, N.; von Rohr, P. R. Extraction in microreactors: Intensification by adding an inert gas phase. *Chem. Eng. Process.* **2011**, *50*, 822−827.
(6) Assmann, N.; Werhan, H.; Ładosz, A.; von Rohr, P. R. Supercritical extraction of lignin oxidation products in a microfluidic device. *Chem. Eng. Sci.* **2013**, *99*, 177−183.
(7) Castell, O. K.; Allender, C. J.; Barrow, D. A. Liquid−liquid phase separation: characterisation of a novel device capable of separating particle carrying multiphase flows. *Lab Chip* **2009**, *9*, 388−396.
(8) Ładosz, A.; von Rohr, P. R. Design rules for microscale capillary phase separators. *Microfluid. Nanofluid.* **2017**, *21*, 153.
(9) Nord, L.; Karlberg, B. Extraction based on the flow-injection principle. *Anal. Chim. Acta* **1980**, *118*, 285−292.

DOI: 10.1021/acs.iecr.7b03207
Ind. Eng. Chem. Res. 2017, 56, 12184−12191

(10) Valcarcel, M.; Luque De Castro, M. D. Continuous separation techniques in flow injection analysis: A review. *J. Chromatogr. A* **1987**, *393*, 3−23.
(11) Jonsson, J. A.; Mathiasson, L. Membrane-based techniques for sample enrichment. *J. Chromatogr A* **2000**, *902*, 205−225.
(12) Cai, Z. X.; Fang, Q.; Chen, H. W.; Fang, Z. L. A microfluidic chip based liquid-liquid extraction system with microporous membrane. *Anal. Chim. Acta* **2006**, *556*, 151−156.
(13) Kralj, J. G.; Sahoo, H. R.; Jensen, K. F. Integrated continuous microfluidic liquid-liquid extraction. *Lab Chip* **2007**, *7*, 256−263.
(14) Adamo, A.; Heider, P. L.; Weeranoppanant, N.; Jensen, K. F. Membrane-based, liquid−liquid separator with integrated pressure control. *Ind. Eng. Chem. Res.* **2013**, *52*, 10802−10808.
(15) Saffarini, R. B.; Mansoor, B.; Thomas, R.; Arafat, H. A. Effect of temperature-dependent microstructure evolution on pore wetting in PTFE membranes under membrane distillation conditions. *J. Membr. Sci.* **2013**, *429*, 282−294.
(16) Borukhova, S.; Noël, T.; Hessel, V. Continuous-Flow Multistep Synthesis of Cinnarizine, Cyclizine, and a Buclizine Derivative from Bulk Alcohols. *ChemSusChem* **2016**, *9*, 67−74.
(17) Dai, C.; Snead, D. R.; Zhang, P.; Jamison, T. F. Continuous-flow synthesis and purification of atropine with sequential in-line separations of structurally similar impurities. *J. Flow Chem.* **2015**, *5*, 133−138.
(18) Gürsel, I. V.; Aldiansyah, F.; Wang, Q.; Noël, T.; Hessel, V. Continuous metal scavenging and coupling to one-pot copper-catalyzed azide-alkyne cycloaddition click reaction in flow. *Chem. Eng. J.* **2015**, *270*, 468−475.
(19) Gürsel, I. V.; Kurt, S. K.; Aalders, J.; Wang, Q.; Noël, T.; Nigam, K. D.; Kockmann, N.; Hessel, V. Utilization of milli-scale coiled flow inverter in combination with phase separator for continuous flow liquid−liquid extraction processes. *Chem. Eng. J.* **2016**, *283*, 855−868.
(20) Hornung, C. H.; Mackley, M. R.; Baxendale, I. R.; Ley, S. V. A microcapillary flow disc reactor for organic synthesis. *Org. Process Res. Dev.* **2007**, *11*, 399−405.
(21) Maurya, R. A.; Min, K.-I.; Kim, D.-P. Continuous flow synthesis of toxic ethyl diazoacetate for utilization in an integrated microfluidic system. *Green Chem.* **2014**, *16*, 116−120.
(22) Noël, T.; Kuhn, S.; Musacchio, A. J.; Jensen, K. F.; Buchwald, S. L. Suzuki-Miyaura Cross-Coupling Reactions in Flow: Multistep Synthesis Enabled by a Microfluidic Extraction. *Angew. Chem.* **2011**, *123*, 6065−6068.
(23) Snead, D. R.; Jamison, T. F. End-to-end continuous flow synthesis and purification of diphenhydramine hydrochloride featuring atom economy, in-line separation, and flow of molten ammonium salts. *Chem. Sci.* **2013**, *4*, 2822−2827.
(24) Snead, D. R.; Jamison, T. F. A three-minute synthesis and purification of ibuprofen: Pushing the limits of continuous-flow processing. *Angew. Chem.* **2015**, *127*, 997−1001.
(25) Tricotet, T.; O'Shea, D. F. Automated Generation and Reactions of 3-Hydroxymethylindoles in Continuous-Flow Microreactors. *Chem. - Eur. J.* **2010**, *16*, 6678−6686.
(26) Varas, A. C.; Noël, T.; Wang, Q.; Hessel, V. Copper (I)-Catalyzed Azide-Alkyne Cycloadditions in Microflow: Catalyst Activity, High-T Operation, and an Integrated Continuous Copper Scavenging Unit. *ChemSusChem* **2012**, *5*, 1703−1707.
(27) Sahoo, H. R.; Kralj, J. G.; Jensen, K. F. Multistep Continuous-Flow Microchemical Synthesis Involving Multiple Reactions and Separations. *Angew. Chem.* **2007**, *119*, 5806−5810.
(28) Alimuddin, M.; Grant, D.; Bulloch, D.; Lee, N.; Peacock, M.; Dahl, R. Determination of log D via Automated Microfluidic Liquid−Liquid Extraction. *J. Med. Chem.* **2008**, *51*, 5140−5142.
(29) Hartman, R. L.; Naber, J. R.; Buchwald, S. L.; Jensen, K. F. Multistep microchemical synthesis enabled by microfluidic distillation. *Angew. Chem., Int. Ed.* **2010**, *49*, 899−903.
(30) Hartman, R. L.; Sahoo, H. R.; Yen, B. C.; Jensen, K. F. Distillation in microchemical systems using capillary forces and segmented flow. *Lab Chip* **2009**, *9*, 1843−1849.
(31) Heider, P. L.; Born, S. C.; Basak, S.; Benyahia, B.; Lakerveld, R.; Zhang, H.; Hogan, R.; Buchbinder, L.; Wolfe, A.; Mascia, S.; Evans, J. M. B.; Jamison, T. F.; Jensen, K. F. Development of a multi-step synthesis and workup sequence for an integrated, continuous manufacturing process of a pharmaceutical. *Org. Process Res. Dev.* **2014**, *18*, 402−409.
(32) Cervera Padrell, A. E.; Morthensen, S. T.; Lewandowski, D. J.; Skovby, T.; Kiil, S.; Gernaey, K. V. Continuous hydrolysis and liquid−liquid phase separation of an active pharmaceutical ingredient intermediate using a miniscale hydrophobic membrane separator. *Org. Process Res. Dev.* **2012**, *16*, 888−900.
(33) Adamo, A.; Beingessner, R. L.; Behnam, M.; Chen, J.; Jamison, T. F.; Jensen, K. F.; Monbaliu, J. C. M.; Myerson, A. S.; Revalor, E. M.; Snead, D. R.; Stelzer, T.; Weeranoppanant, N.; Wong, S. Y.; Zhang, P. On-demand continuous-flow production of pharmaceuticals in a compact, reconfigurable system. *Science* **2016**, *352*, 61−67.
(34) Peer, M.; Weeranoppanant, N.; Adamo, A.; Zhang, Y.; Jensen, K. F. Biphasic Catalytic Hydrogen Peroxide Oxidation of Alcohols in Flow: Scale-up and Extraction. *Org. Process Res. Dev.* **2016**, *20*, 1677−1685.
(35) Weeranoppanant, N.; Adamo, A.; Saparbaiuly, G.; Rose, E.; Fleury, C.; Schenkel, B.; Jensen, K. F. Design of Multistage Counter-Current Liquid−Liquid Extraction for Small-Scale Applications. *Ind. Eng. Chem. Res.* **2017**, *56*, 4095−4103.
(36) Bharadwaj, R. K. Modeling the Barrier Properties of Polymer-Layered Silicate Nanocomposites. *Macromolecules* **2001**, *34*, 9189−9192.
(37) Kreulen, H.; Smolders, C. A.; Versteeg, G.; Van Swaaij, W. Determination of Mass Transfer Rates in Wetted and Non-Wetted Microporous Membranes. *Chem. Eng. Sci.* **1993**, *48*, 2093−2102.
(38) Roydhouse, M. D.; Pradas, M.; Al-Rifai, N.; Azizi, B.; Cao, E. H.; Kalliadasis, S.; Gavriilidis, A. Operating ranges of gas-liquid capillary microseparators: Experiments and theory. *Chem. Eng. Sci.* **2014**, *114*, 30−39.

DOI: 10.1021/acs.iecr.7b03207
Ind. Eng. Chem. Res. 2017, 56, 12184−12191